High-order sliding mode control of rotor-side converter in doubly-fed wind power generation system

Mohammad Ali karami*[a], Seyed Mohammad Shariatmadar[a], Mohammad Esmaeil Nazari[b], Javad Rahmani-Fard[c]

[a] *Naragh Branch, Islamic Azad University, 58719-37961, Naragh, Iran,*
[b] *Golpayegan University of Technology, 38181-46763, Golpayegan, Iran, ,*
[c] *Pooyesh Institute of Higher Education,37167-15114, Qom, Iran,*

E-mail addresses and Tel: karami.mohammad.ali97@gmail.com, +989163644311 (M. A. karami); shariatmadar@gmail.com, +989124522967 (S. M. Shariatmadar); menazari@aut.ac.ir, +989188664386 (M. E. Nazari); rahmanifard@qut.ac.ir, +989120517088 (J. Rahmani-Fard)

Abstract

This paper proposes a high-order sliding mode control strategy to improve the performance of power decoupling control for double-fed induction generators (DFIG). Initially, the mathematical model of DFIGs is analyzed based on the principle of voltage-oriented vector control. DFIGs efficient operation is vital for grid stability and power quality. However, these generators are susceptible to disturbances and uncertainties, which can affect their performance. To address this issue and poor dynamic performance of traditional control methods in achieving power decoupling and the nonlinearity of the wind turbine model, the proposed control method utilizes high-order sliding mode controller using power function approaching law. Simulation results demonstrate that the proposed control approach outperforms traditional PI controllers in terms of accuracy, robustness, and dynamic and static performance. A series of experiments, including no-load grid connection and power decoupling control, were successfully conducted on this platform. Analysis of the experimental waveforms for independent adjustment of active and reactive power shows that when either the active or reactive power is independently changed, the other power remains relatively constant. Therefore, the experimental results verified that the grid-connected power control strategy of the system can achieve dynamic decoupling control between active and reactive power.

***Keywords**:* DFIG; Decoupling control; Power function; High-order sliding mode, Nonlinear Control

---

1. Introduction

The decoupling control of active and reactive power under dynamic conditions is a prerequisite for stable operation and grid connection of DFIGs in wind power systems. Its control effect directly affects the performance of the power generation system. The power decoupling control of the DFIG system is implemented through the rotor-side converter, so effective control of it is particularly important.

Reference [1] proposes a double-closed-loop PI control strategy based on vector control, which achieves decoupling of power under dynamic conditions of the DFIG system. However, the control effect of the system is easily affected by the motor parameters, and it is difficult to tune the controller parameters. Reference [2] proposes an improved multi-loop adaptive control method based on disturbance observer, which achieves maximum wind energy tracking and power decoupling. However, its dynamic performance depends heavily on the PI controller parameters. Reference [3] proposes a composite sliding mode control strategy, which solves the problem that the system control

---

The present address of **Mohammad Ali karami** and **Seyed Mohammad Shariatmadar is**: *Department of Electrical Engineering, College of Engineering, Khomein Branch, Islamic Azad University, Khomein, Iran.*
The present address of **Javad Rahmani-Fard** is: *Departmanet of Electerical and Computer Engineering, Qom University of Technology, Qom, Iran.*

effect is easily affected by the motor parameters, but the switching function characteristic in the control law makes the shaking phenomenon still unresolved after the system enters a steady state, and the dynamic performance and robustness of the system will also be affected. Reference [4] proposes a novel robust rotor current sensorless control scheme, which achieves power decoupling control of the system by adjusting the stator current. However, due to the connection between the power grid and the stator, its control effect will be severely reduced during power grid faults.

An advanced control strategy, for permanent magnet direct drive wind energy conversion systems (WECS) is proposed in [5]. This strategy combines maximum power point tracking (MPPT) and optimal torque control (OTC), utilizing artificial neural networks (ANN) for intelligent tracking range. It aims to enhance the performance and efficiency of the WECS by efficiently controlling the torque and maximizing power output.

The several advanced control techniques for WECS that utilize DFIG are discussed in [6]. These techniques focus on enhancing the performance and stability of DFIG-based WECS by addressing challenges such as grid integration, power quality, and optimal power extraction. The study explores various control approaches including model predictive control (MPC), fuzzy logic control (FLC), and ANN to improve the overall efficiency and reliability of DFIG-based WECS. Reference [7] proposes the integration of ANN with Direct Power Control to improve the performance and efficiency of DFIG-based WECS by mitigating the impact of parameter variations and non-linearities, leading to more accurate and responsive control of active and reactive power.

A comparative study of MPPT controllers for WECS is introduced in [8] .Different MPPT techniques, such as perturb and observe (P&O), incremental conductance, and FLC, are analyzed and evaluated in terms of their performance and effectiveness in capturing the maximum power from the wind turbine. The study provides insights into the advantages and limitations of each controller, aiding in the selection and implementation of an optimal MPPT strategy for WECS applications.

The application of sliding mode and terminal sliding mode control techniques for cascaded DFIGs are studied in [9]. The study explores control strategies to enhance the performance and stability of DFIGs in wind power systems.

Reference [10] proposes a global integral sliding mode control strategy for the harmonic detection delay and poor harmonic current tracking accuracy and poor robustness of active parallel power filters. In order to achieve the goal of weakening the shaking, the sign function in the sliding mode approaching law is replaced by a continuous saturation function. Although the shaking phenomenon is significantly improved, the shaking still exists after the system reaches a steady state. Reference [11] proposes a continuous high-order sliding mode control strategy for the torque control problem of wind turbines when the wind speed is lower than the rated wind speed, but the parameters in its control law are not easy to determine, and poor setting will make the system unstable. Reference [12] proposes a high-order sliding mode control strategy based on vector control principles, but the high-frequency shaking caused by the sign function characteristic in the index approaching law will result in poor decoupling control effect of the DFIG system, and the maximum wind energy tracking will also be affected. Reference [13] introduces the $fal(x, \alpha, \delta)$ function into sliding mode control and designs a sliding mode control algorithm based on power-law approaching, which shows good dynamic and static quality and small shaking in simulation results. Therefore, this paper introduces high-order sliding mode control based on the nonlinear $fal(x, \alpha, \delta)$ function approaching law into the DFIG system to improve the control effect and dynamic and static performance of the system.

2. Mathematical Model of DFIG

The stator of the DFIG is directly connected to the grid, and the rotor is connected to the AC excitation power supply. The control of the motor speed or power can be realized by controlling the rotor current. In this paper, when establishing the mathematical model of the DFIG, both the stator and rotor windings adopt the motor convention, and the current of the stator and rotor windings is positive for the inflow, so its mathematical model under the two-phase synchronous rotating coordinate system (dq) is as follows [14-15]:

stator winding voltage equation is:

$$\begin{cases} u_{sd} = R_s i_{sd} + \dfrac{d\psi_{sd}}{dt} - \omega_1 \psi_{sq} \\ u_{sq} = R_s i_{sq} + \dfrac{d\psi_{sq}}{dt} + \omega_1 \psi_{sd} \end{cases} \tag{1}$$

Rotor winding voltage equation is:

$$\begin{cases} u_{rd} = R_r i_{rd} + \dfrac{d\psi_{rd}}{dt} - \omega_s \psi_{rq} \\ u_{rq} = R_r i_{rq} + \dfrac{d\psi_{rq}}{dt} + \omega_s \psi_{rd} \end{cases} \tag{2}$$

where, $u_{sd}, u_{sq}, u_{rd}, u_{rq}$ are the d-axis and q-axis components of the stator and rotor voltage respectively; $i_{sd}, i_{sq}, i_{rd}, i_{rq}$ are the d and q axis components of the stator and rotor currents respectively; $\psi_{sd}, \psi_{sq}, \psi_{rd}, \psi_{rq}$ are the d and q axes components of the stator and rotor flux linkages respectively; R_s and R_r are stator and rotor resistance respectively. ω_1 is the synchronous rotation speed of the stator magnetic field; $\omega_s = \omega_1 - \omega_r$ is the slip angular frequency, and ω_r is the electrical angular frequency of the rotor.

Stator flux equation is:

$$\begin{cases} \psi_{sd} = L_s i_{sd} + L_m i_{rd} \\ \psi_{sq} = L_s i_{sq} + L_m i_{rq} \end{cases} \tag{3}$$

Rotor flux equation is:

$$\begin{cases} \psi_{rd} = L_r i_{rd} + L_m i_{sd} \\ \psi_{rq} = L_r i_{rq} + L_m i_{sq} \end{cases} \tag{4}$$

in which L_s, L_r are the self-inductance of the stator and rotor respectively; L_m mutual inductance between stator and rotor windings.

The stator output power equation is:

$$\begin{cases} P_s = 1.5\left(u_{sd} i_{sd} + u_{sq} i_{sq}\right) \\ Q_s = 1.5\left(u_{sq} i_{sq} - u_{sd} i_{sd}\right) \end{cases} \tag{5}$$

in which P_s and Q_s are the active and reactive power of the stator side respectively.

The electromagnetic torque equation is:

$$T_e = 1.5 n_p L_m \left(i_{sq} i_{sd} - i_{sd} i_{sq}\right) \tag{6}$$

in which T_e is the electromagnetic torque; n_p is the number of pole pairs.

The equation of motion is:

$$T_e - T_L = \frac{J}{n_p} \cdot \frac{d\omega_r}{dt} \tag{7}$$

in which T_L is the driving torque provided by the wind turbine; J is the moment of inertia.

3. Stator Voltage Oriented Vector Control and maximum wind energy tracking

Fig.1 shows spatial position between three -phase (*abc*) coordinate system and two-phase rotating (*dq*) coordinate system. The stator three-phase stationary coordinate system is represented by $a_1b_1c_1$. The rotor three-phase coordinate system is represented by $a_2b_2c_2$, and it rotates counter clockwise at the angular velocity ω_r. Moreover, θ_r is the angle between the a_2 axis and the a_1 axis, and θ_s is the angle between *d* axis and the a_1 axis.

Fig. 1.

If the stator voltage vector u_s coincides with the direction of the d axis, then the components of the voltage on the *d* axis and the *q* axis are respectively $u_{sd} = u_s$ and $u_{sq} = 0$. When the DFIG system runs stably, the stator winding resistance is much smaller than the stator winding inductance, which can be ignored, that is, $R_s = 0$. Moreover, since the induced electromotive force vector of the generator lags the stator flux linkage $\measuredangle \psi_s = 90^\circ$, ψ_s is in the positive direction of the q-axis, so $\psi_{sd} = 0$, $\psi_{sq} = \psi_s$. Substituting $R_s = 0$, $u_{sd} = u_s$, $u_{sq} = 0$ and $\psi_{sd} = 0$, $\psi_{sq} = \psi_s$ into Eq. (1) and Eq. (3) to get:

$$\begin{cases} \psi_s = -\dfrac{u_s}{\omega_1} \\ \dot{\psi}_s = 0 \end{cases} \tag{8}$$

$$\begin{cases} i_{rd} = -\dfrac{L_s i_{sm}}{L_m} \\ i_{rq} = \dfrac{-L_s i_{st} + \psi_s}{L_m} \end{cases} \tag{9}$$

Substituting Eq. (9) into rotor flux Eq. (4) to get:

$$\begin{cases} \psi_{rd} = -L_m \dfrac{L_m i_{rd}}{L_s} + L_r i_{rd} = \sigma i_{rd} \\ \psi_{rq} = L_m \left(\dfrac{\psi_s - L_m i_{rq}}{L_s} \right) + L_r i_{rq} = \sigma i_{rq} + \dfrac{L_m}{L_s} \psi_s \end{cases} \tag{10}$$

where $\sigma = L_r - \left(L_m^2 / L_s \right)$. Substituting Eq. (10) into Eq. (2), we can get:

$$\begin{cases} u_{rd} = u'_{rd} + \Delta u_{rd} \\ u_{rq} = u'_{rq} + \Delta u_{rq} \end{cases} \tag{11}$$

Where

$$\begin{cases} u'_{rd} = R_r i_{rd} + \sigma \dfrac{di_{rd}}{dt} \\ u'_{rq} = R_r i_{rq} + \sigma \dfrac{di_{rq}}{dt} \end{cases} \tag{12}$$

$$\begin{cases} \Delta u_{rd} = -\omega_s \dfrac{L_m}{L_s} \psi_s - \omega_s \sigma i_{rq} \\ \Delta u_{rq} = \omega_s \sigma i_{rd} \end{cases} \tag{13}$$

in which u'_{rd} , u'_{rq} are rotor voltage decoupling items; Δu_{rd}, Δu_{rq} are rotor voltage compensation items. Substituting $u_{sd} = u_s$ and $u_{sq} = 0$ into Eq. (5), we can get:

$$\begin{cases} P_s = 1.5 u_s i_{sd} \\ Q_s = -1.5 u_s i_{sq} \end{cases} \tag{14}$$

As per equation (14), it can be inferred that under the stator voltage directional control, the active and reactive power of the system are solely dependent on the stator currents, i_{sd}, i_{sq} . Furthermore, since there exists a relationship between i_{sd}, i_{sq} , and rotor currents i_{rd}, i_{rq} as stipulated in equation (9), controlling i_{rd}, i_{rq} enables independent regulation of active and reactive power. This, in turn, achieves the objective of decoupling.

There is a maximum output power point P_{max} on the optimal power curve of the wind turbine. When it is equal to the output power P_m of the wind turbine, that is, $P_{\max} = P_m = k_w \omega_m^3$ and the maximum tracking of wind energy is realized [16]. The output active power of the stator at this time is the reference value of active power, that is, $P_s^* = P_s$. According to the theory of DFIG, and with the assumption that the mechanical losses of the wind turbine and the copper losses of the stator and rotor are negligible, the active power reference value of the DFIG system can be calculated as follows:

$$P_s^* = \frac{P_{\max}}{1-s} = \frac{k_w \omega_m^3}{1-s} \tag{15}$$

Where, $k_w = 0.5 \rho S_w \left(R/\lambda_m\right)^3 C_{pmax}$ is the basic constant related to the wind turbine; ω_m is the speed of the wind turbine; ρ is the air density; S_w is the swept area of the wind turbine blade; R is the radius of the wind turbine; λ_m is the optimal tip speed ratio (the rotor blade tip speed to wind speed); C_{pmax} is the maximum utilization coefficient of wind energy.

4. Design of high-order sliding mode controller based on reaching law of power function

The overall control block diagram of the system is shown in Fig. 2 . Sliding mode control is a nonlinear control method that has advantages such as flexible structure, strong robustness, and fast response [17, 18]. However, its downside is that after entering the sliding surface, the system's motion trajectory does not approach the centre equilibrium point in a relatively smooth way but rather oscillates back and forth on both sides of the sliding surface, resulting in chattering. Chattering can affect the system's performance, making it a focus of research in sliding mode control. The design of the switching surface in traditional sliding mode control is limited by the order of the system variables, which limits the control to some extent. However, high-order sliding mode switching surface design is not limited by this order limitation and inherits the advantages of traditional sliding mode structures such as flexibility, fast response, and strong anti-interference ability while significantly improving the system's control accuracy and chattering [16]. Typically, there is a sign function in the reaching law of sliding mode control, which inevitably causes chattering in the system. Usually, the sign function is replaced with a saturation function to suppress high-frequency chattering in the system. However, chattering still exists after the system reaches steady-state. Nonlinear power functions exhibit excellent properties that not only converge but also improve the chattering problem of the system [19].

Fig. 2.

4.1. Nonlinear power function

The expression of nonlinear power function [20] is

$$fal(x,\alpha,\delta)=\begin{cases}\dfrac{x}{\delta^{1-\alpha}}, & |x|\le\delta;\\ sign(x).|x|^{\alpha}, & |x|>\delta.\end{cases} \tag{16}$$

In which, $0<\alpha<1$, $0<\delta<1$. Fig. 3 shows the relationship curve between the power function, sign function, and saturation function (*sat*( )) when $\alpha=$ 0.01 and $\delta=0.05$. As can be seen from Figure 3, within the error range of $e\in(-0.05,\ 0.05)$, the gain of the nonlinear power function is between the gains of the sign function and the saturation function. However, when $e\in(0.05,\ 0.15)$ or $e\in(-0.15,\ -0.05)$, the gain of the power function is greater than both the sign function and the saturation function, fully reflecting the "small gain for large errors, large gain for small errors" characteristic [21].

Fig. 3.

4.2. High-order sliding mode controller design

The active and reactive power errors of the DFIG system are defined as:

$$\begin{cases}e_P=P_s^*-P_s\\ e_Q=Q_s^*-Q_s\end{cases} \tag{17}$$

In which, Q_s^* is the reference value of reactive power, which is directly given in this paper.
Substituting Eq. (14) into Eq. (17) and deriving:

$$\begin{cases}\dot{e}_P=\dot{P}_s^*-1.5u_s\,\dot{i}_{sd}\\ \dot{e}_Q=\dot{Q}_s^*+1.5u_s\,\dot{i}_{sq}\end{cases} \tag{18}$$

From Eq. (8) and Eq. (9):

$$\begin{cases} \dot{e}_P = \dot{P}_s^* + 1.5u_s \dfrac{L_m}{L_s} \dot{i}_{rd} \\ \dot{e}_Q = \dot{Q}_s^* - 1.5u_s \dfrac{L_m}{L_s} \dot{i}_{rq} \end{cases} \tag{19}$$

Substituting Eq. (4) into Eq. (2), and then according to Eq. (9), we can get:

$$\begin{cases} \dot{e}_P = \dot{P}_s^* + 1.5u_s \dfrac{L_m}{L_s} \dfrac{u_{rd} - R_r i_{rd} + \omega_s \psi_{rq}}{\sigma L_s} \\ \dot{e}_Q = \dot{Q}_s^* + 1.5u_s \dfrac{L_m}{L_s} \dfrac{u_{rq} - R_r i_{rq} - \omega_s \psi_{rd}}{\sigma L_s} \end{cases} \tag{20}$$

The sliding mode switching function is designed as:

$$\begin{cases} s_1 = e_P + \alpha_1 \dot{e}_P \\ s_2 = e_Q + \alpha_2 \dot{e}_Q \end{cases} \tag{21}$$

In which, $0 < \alpha_1 < 1$ and $0 < \alpha_2 < 1$. Taking the derivative of Eq. (21), we can get:

$$\begin{cases} \dot{s}_1 = \dot{e}_P + \alpha_1 \ddot{e}_P \\ \dot{s}_2 = \dot{e}_Q + \alpha_2 \ddot{e}_Q \end{cases} \tag{22}$$

The reaching law for a nonlinear power function is as follows:

$$\begin{cases} \dot{s}_1 = -k_1 s_1 - k_2 fal\left(s_1, \alpha, \delta\right) \\ \dot{s}_2 = -k_3 s_2 - k_4 fal\left(s_2, \alpha, \delta\right) \end{cases} \tag{23}$$

In which, $k_1 > 0, k_2 > 0, k_3 > 0, k_4 > 0$. Then from Eq. (22) and Eq. (23), we can get:

$$\begin{cases} \dot{e}_P = \dfrac{1}{\alpha_1} \displaystyle\int_0^t \left(-k_1 s_1 - k_2 fal\left(s_1, \alpha, \delta\right) - \dot{e}_P\right) d\tau \\ \dot{e}_Q = \dfrac{1}{\alpha_2} \displaystyle\int_0^t \left(-k_3 s_2 - k_4 fal\left(s_2, \alpha, \delta\right) - \dot{e}_Q\right) d\tau \end{cases} \tag{24}$$

Combined with Eq. (20), the control law can be obtained:

$$\begin{cases} u_{rd} = u_{rdn} + \Delta u_{rd} \\ u_{rq} = u_{rqn} + \Delta u_{rq} \end{cases} \tag{25}$$

where,

$$\begin{cases} \Delta u_{rd} = -\omega_s \psi_{rq} = -\omega_s \dfrac{L_m}{L_s} \psi_s - \omega_s \sigma i_{rq} \\ u_{rdn} = R_r + i_{rd} + \dfrac{\dfrac{\sigma L_s}{\alpha_1} \displaystyle\int_0^t \left(-k_1 s_1 - k_2 fal\left(s_1, \alpha, \delta\right) - \dot{e}_P\right) d\tau - \sigma L_s \dot{P}_s^*}{1.5u_s L_m} \end{cases} \tag{26}$$

$$\begin{cases} \Delta u_{rq} = \omega_s \psi_{rd} = \omega_s \sigma i_{rd} \\ u_{rqn} = R_r i_{rq} + \dfrac{\dfrac{\sigma L_s}{\alpha_2} \displaystyle\int_0^t \left(-k_3 s_2 - k_4 fal\left(s_2, \alpha, \delta\right) - \dot{e}_Q\right) d\tau - \sigma L_s \dot{Q}_s^*}{1.5 u_s L_m} \end{cases} \tag{27}$$

4.3. Stability Proof

The Lyapunov function is chosen to prove the stability of the designed system:

$$v = \frac{1}{2} s_1^2 \tag{28}$$

and take derivatives with respect to time:

$$\begin{aligned} \dot{v} &= s_1 \dot{s}_1 = s_1\left(\dot{e}_P + \alpha_1 \ddot{e}_P\right) = s_1\left(\dot{e}_P + \alpha_1\left(\ddot{P}_s^* + \ddot{P}_s\right)\right) = s_1\left(\dot{e}_P + \alpha_1\left(\ddot{P}_s^* - 1.5 u_s \ddot{i}_{sd}\right)\right) \\ &= s_1\left(\dot{e}_P + \alpha_1\left(\ddot{P}_s^* + 1.5 u_s \frac{L_m}{L_s} \ddot{i}_{rd}\right)\right) = s_1\left(\dot{e}_P + \alpha_1\left(\ddot{P}_s^* + 1.5 u_s \frac{L_m}{\sigma L_s}\left(\dot{u}_{rd} - R_r \dot{i}_{rd} + \omega_s \dot{\psi}_{rq}\right)\right)\right) \\ &= s_1\left(-k_1 s_1 - k_2 fal\left(s_1, \alpha, \delta\right)\right) \end{aligned} \tag{29}$$

When $s_1 > 0$, $\dot{v} = s_1\left(-k_1 s_1 - k_2 fal\left(s_1, \alpha, \delta\right)\right) < 0$; and when $s_1 < 0$, $\dot{v} = s_1\left(-k_1 s_1 - k_2 fal\left(s_1, \alpha, \delta\right)\right) < 0$. Therefore, for any s_1 , $\dot{v} < 0$, and the system satisfies the Lyapunov stability condition, so the system is asymptotically stable. The stability of s_2 can also be proved by the above theory.

5. System simulation analysis

Using the Matlab/Simulink simulation, the proposed control strategy is verified and compared with the DFIG system based on PI control. The parameters of investigated the wind turbine are listed in Table 1.

Table. 1

In the designed controller $k_1 = k_3 = 0.1$, $k_2 = k_4 = 400$, moreover in the power function $\alpha =$ 0.01 , $\delta =$ 0.05 .

5.1. Maximum wind power tracking of DFIG system based on high-order sliding mode control of power function

Given an initial wind speed of 8 m/s, a simulation time of 1 s, and a sudden change in wind speed to 10 m/s at 0.5 s, the curves of various parameters of the DFIG system are shown in Fig.4 and Fig.5. Using the optimal electrical angular velocity formula [22-23] $\omega_r = n_p \lambda_m \left(kv / R\right)$, the theoretical values of the electrical angular velocities are calculated to be 333.6 rad/s and 417.1 rad/s for wind speeds of 8 m/s and 10 m/s, respectively.

Fig. 4.

Fig. 5.

As shown in Fig. 4, due to the change in wind speed, the electromagnetic torque of the DFIG changes from -15 *N.m* to -31.6 *N.m*; the driving torque provided by the wind turbine also changes from 15 *N.m* to 31.6 *N.m*. As shown in Fig. 5, when the wind speed changes, the actual value of the active power of the DFIG system based on both PI control and power function high-order sliding mode control, as well as the reference value of the active power P_s^*, change accordingly. It can be seen from Fig. 5 that the actual value of the stator output active power changes with the wind speed and is basically consistent with the reference value calculated by Eq. (18) when the system is in a steady state, indicating that both control methods can achieve maximum wind power tracking. However, the reference and actual values of the active power under PI control will have significant fluctuations when the system tends to be stable or when the wind speed changes, while the reference and actual values of the active power under sliding mode control not only fluctuate less but also quickly stabilize, reflecting good dynamic performance. As shown in Fig. 6, given an initial wind speed of 8 m/s, a simulation time of 1 *s*, and a change in rotor resistance from 2.57 Ω to 1.57 Ω at 0.5 s, it can be clearly seen that when the rotor resistance changes, the active power of both the DFIG system based on PI control and the DFIG system based on power function high-order sliding mode control will briefly change before stabilizing. However, the active power of the DFIG system based on power function high-order sliding mode control changes more quickly and with smaller fluctuations, demonstrating better robustness.

Fig. 6.

5.2. Power decoupling of DFIG system under PI and sliding mode control

As shown in Fig. 7, the simulation time is 1.5 seconds, and the wind speed changes from 8 m/s to 10 m/s and then to 12 m/s at 0.5 s and 1 s, respectively. At 0.8 s, the reactive power set value changed from 1250 var to 2000 var, and then decreased to 1550 var at 1.3 s. The changes of active and reactive power of DFIG system under two control methods are as follows: From Fig. 7(a), it can be seen that when the wind speed changes at 0.5 s and 1 s, the system's active power will change with the wind speed, while the reactive power remains unchanged. From Fig. 7(b), it can be seen that the change of reactive power at 0.8 s and 1.3 s does not affect the active power of the system, so the power decoupling under dynamic conditions is achieved. However, it is obvious that the fluctuation of active power under PI control is higher than that under high-order sliding mode control based on power function, and the adjustment time is relatively long. Analysis shows that the dynamic performance of high-order sliding mode control strategy based on power function is better than that of traditional PI control strategy.

Fig. 7.

6. Experimental results

Based on the topology structure of the doubly-fed wind power simulation system described in Section (2), an experimental platform is built. An asynchronous motor is used as the prime mover to simulate wind speed, and a doubly-fed motor is used to drag it into grid-connected power generation. Based on the control strategy in this paper, software programs are written and executed for the back-to-back converter system for system debugging, and wind power simulation system related control experiments are implemented. Finally, through analysis and comparison of the experimental results, the actual performance of the wind power simulation system and the reliability of the software algorithms used are verified. The physical experiment platform is shown in Fig. 8. The main electrical parameters of the simulation platform are listed in Table 2.
In a doubly-fed wind turbine simulation system, a DFIG and an asynchronous motor form a coaxial drivetrain. The asynchronous motor is controlled by a frequency converter to realize wind speed simulation. the parameters of the

DFIG and asynchronous motor are as follows:
1) DFIG: model YSF112M-5, rated power 3kW, rated stator voltage 380V, number of motor pole pairs: 2, rated speed 1800r/min, stator resistance 1.92Ω, rotor impedance 2.58Ω, stator and rotor inductance 0.25H, mutual inductance coefficient 0.156H.
2) AC asynchronous motor: model YVP112M-2, rated power 4KW, rated current 8A, speed range 0~2800r/min;
3) ABB inverter: model ACS510, rated power 10KW.

Table. 2

The experimental content in this topic can be divided into two parts: Back-to-back converter system function debugging and wind power simulation system machine experiment. Back-to-back converter system function debugging is to verify the feasibility and reliability of its hardware implementation and software design, find system defects and improve them through experiments, and verify whether the system meets the performance indicators. The whole machine experiment of the wind power simulation system is a verification experiment, the purpose is to simulate the actual working state of the wind power system, to realize and verify control strategy of the doubly-fed wind power system proposed in this paper, as well as the variable speed and constant frequency operation, etc.

Fig.8.

In order to verify the actual effect of the proposed control strategy, the experiment was carried out, in which the traditional control strategy fixed PI parameters. The control quality of the two control strategies is observed through the experimental results, and the experiments are carried out under two conditions of stable wind speed and variable wind speed. After the double-fed wind power simulation system is connected to the grid, the stator voltage is equal to the grid voltage. At this time, it is necessary to control the active power and reactive power of the stator side. According to the characteristics of the doubly-fed wind power simulation system in the experiment, the grid-connected operation experiment with given power and the independent decoupling control experiment of active and reactive power were carried out.

6.1. Grid-connected operation under different wind speed conditions

The grid-connected operation experiment with given power under different wind speed conditions is a test of the doubly-fed wind power simulation system in different steady states. The operating characteristics under the wind speed are verified, and the parameters given in the experiment are shown in Table 3.

Table. 3

It can be seen from Fig. 9 that when the wind speed set point is changed, the amplitude and phase of the stator current remain basically unchanged, indicating that the stator power remains basically stable. The stator-side power waveform is shown in Fig.10. Since the power waveforms at three steady-state wind speeds are the same, only the sub-synchronous speed stator-side power waveform is plotted.

Fig.9.

Fig.10.

6.2. Grid-connected operation under wind speed variation

The power-given grid-connected operation experiment under wind speed variation is a simulation experiment conducted on a doubly-fed wind power simulation system under conditions of severe wind speed variation after being grid-connected. The purpose of the experiment is to verify the control strategy and performance of the Back-to-back converter system. The wind speed variation range is selected between sub-synchronous and super-synchronous speeds. In the experiment, the wind speed is controlled by a frequency converter controlling the asynchronous machine. System parameters are given in Table 4 during the experiment.

Table 4.

The rotor current waveform during the process of wind speed change is shown in Fig.11. According to the analysis of the rotor current waveform in Fig.11, it can be observed that when a DFIG switches between sub-synchronous speed at 700r/min and super-synchronous speed at 1700r/min, the frequency of the rotor current changes with the wind speed. For example, in Fig.11 (a), when the wind speed is at 700r/min, the frequency of the rotor current is 26.7Hz, which decreases as the wind speed increases. When the wind speed approaches synchronous speed at 1500r/min, the frequency of the rotor current becomes zero, and the rotor current is close to direct current. When the wind speed reaches super-synchronous speed at 1700r/min, the rotor current undergoes commutation, and the frequency increases to 6.67Hz, while the DC bus voltage remains stable at 650V during the wind speed variation experiment. This shows that when the wind speed switches between sub-synchronous and super-synchronous operating states, the rotor current can be smoothly and stably commutated and varied in frequency by the control strategy of the rotor converter, thus achieving smooth and stable variable speed constant frequency operation of the doubly-fed wind power simulation system.

Fig.11.

The AC input voltage and current waveforms of the grid-side in the wind speed variation experiment are shown in Fig.12. It can be observed that as the wind speed changes from sub-synchronous speed to super-synchronous speed, the phase of the grid-side converter voltage and current changes, and the grid-side converter switches between rectification and inversion, which means that the control strategy of the grid-side converter achieves bidirectional flow of energy. Due to the fact that the stator voltage, current, and power waveforms before and after wind speed changes are basically the same as the steady-state experimental waveforms under different wind speed conditions, the stator-side power remains constant during the wind speed change experiment, so their experimental waveforms are not listed in detail. Therefore, according to the steady-state wind speed and wind speed change experiments in grid-connected operation, the doubly-fed wind power simulation system can achieve stable grid-connected operation under different steady-state wind speed conditions, ensuring the stable output power of the stator side. This verifies the basic operating principle and system performance of the DFIG, and demonstrates the ability of the back-to-back converter system to automatically change the operating conditions of the grid-side and rotor-side converters according to the different working conditions of the DFIG. It also verifies the bidirectional flow of energy in the rotor circuit and the principle of variable speed constant frequency operation. At the same time, the wind speed variation experiment simulates the case of severe wind speed changes in actual wind power systems, verifying the control performance of the simulation system during severe wind speed changes and indirectly testing the reliability of the back-to-back converter system platform.

Fig.12.

6.3. Active and reactive power independent decoupling control

The experiment was conducted in two parts based on independent adjustment of active and reactive power, with the system parameters given as shown in Table 5.

Table 5.

In the stator-side independent active power regulation experiment, the reactive power was set to zero, and the stator-side active power was independently adjusted while observing the changes in stator voltage, current, and power. The experimental waveforms are shown in Fig.12 and Fig.13. From the experimental waveforms, it can be seen that when the stator-side active power is changed, the reactive power remains relatively constant, and the amplitude of the stator current increases or decreases with the increase or decrease of the active power, respectively. Thus, the experiment successfully achieved independent regulation of stator-side active power.

Fig.12.

Fig.13.

In the stator-side independent reactive power regulation experiment, the active power was set to 2000W, and the stator-side reactive power was independently adjusted while observing the changes in stator voltage, current, and power. The experimental waveforms are shown in Fig.14 and Fig.15. As can be seen, it can be seen that when the stator-side reactive power is changed, the active power remains relatively constant, and the amplitude and phase of the stator current vary with the change in reactive power. When the reactive power is positive, the stator current lags behind the stator voltage, and vice versa. Thus, the experiment successfully achieved independent regulation of stator-side reactive power. Analysis of the experimental waveforms for independent adjustment of stator-side active and reactive power shows that when either the active or reactive power is independently changed, the other power remains relatively constant. Therefore, the experimental results verified that the grid-connected power control strategy of the system can achieve dynamic decoupling control between active and reactive power. This experiment also provides a basis for future experiments to dynamically change the setpoint of active and reactive power based on grid demand in the wind power simulation system.

Fig.14.

Fig.15

7. Conclusion

This paper presents an improved version of the control strategy for dynamic decoupling of active and reactive power in DFIG systems. The proposed approach utilizes a high-order sliding mode control strategy based on the power function reaching law. By combining the principles of stator voltage-oriented vector control and sliding mode control theory, the control strategy effectively addresses the challenges posed by variable wind conditions and grid disturbances in wind power generation systems. The control strategy includes the derivation of the rotor converter for grid connection and the development of a stator power decoupling control strategy based on voltage-oriented vector control. The integration of higher-order sliding mode control on the rotor-side converter enhances the overall performance of the wind power generation system. Simulation experiments and real-world tests were conducted to validate the effectiveness and superiority of the proposed control method. The results demonstrate that the proposed approach successfully mitigates the negative impact of wind speed variations, improving the overall power performance of the DFIG system. Overall, this study provides valuable insights into enhancing the control strategy for DFIG systems in wind power generation, offering practical solutions for optimizing system performance in the face of variable operating conditions and grid disturbances.

References

[1] Kerrouche, K., Mezouar, A. and Belgacem, K. “Decoupled control of doubly fed induction generator by vector control for wind energy conversion system”, *Energy procedia*, **42**, pp.239-248 (2013).

[2] Lin, X., Xiahou, K., Liu, Y. and et al. “Design and hardware-in-the-loop experiment of multiloop adaptive control for DFIG-WT”, *IEEE Transactions on Industrial Electronics*, **65**(9), pp.7049-7059 (2018).

[3] Sami, I., Ullah, S., Ullah, N. and et al. “Sensorless fractional order composite sliding mode control design for wind generation system”. *ISA transactions*, **111**, pp.275-289 (2021).
[4] Xiahou, K., Lin, X., Liu, Y. and et al. “Robust rotor-current sensorless control of doubly fed induction generators”, *IEEE Transactions on Energy Conversion*, **33**(2), pp.897-899 (2018).
[5] Meghni, B., Chojaa, H. and Boulmaiz, A. “December. An optimal torque control based on intelligent tracking range (MPPT-OTC-ANN) for permanent magnet direct drive WECS”, *In 2020 IEEE 2nd International Conference on Electronics, Control, Optimization and Computer Science (ICECOCS)*, pp. 1-6 (2020).
[6] Chojaa, H., Derouich, A., Chehaidia, S.E., and et al. “Advanced control techniques for doubly-fed induction generators based wind energy conversion systems”, *In 2022 Global Energy Conference (GEC)*, pp. 282-287 (2022).
[7] Chojaa, H., Derouich, A., Chehaidia, S.E., and et al. “Enhancement of Direct Power Control by Using Artificial Neural Network for a Doubly Fed Induction Generator-Based WECS: An Experimental Validation”, *Electronics*, **11**(24), p.4106.
[8] Chojaa, H., Derouich, A., Bourkhime, Y., and et al. “Comparative study of MPPT controllers for a wind energy conversion system”, *InInternational Conference on Advanced Technologies for Humanity, Cham: Springer International Publishing*, pp. 300-310 (2021).
[9] Abdolhadi, H.Z., Markadeh, G.A., Boroujeni, S.T., “Sliding Mode and Terminal Sliding Mode Control of Cascaded Doubly Fed Induction Generator”, *Iranian Journal of Electrical & Electronic Engineering*, **17**(3), (2021).
[10] Tareen, W.U.K., Aamir, M., Mekhilef, S., and et al. “Mitigation of power quality issues due to high penetration of renewable energy sources in electric grid systems using three-phase APF/STATCOM technologies: A review”, *Energies*, **11**(6), p.1491 (2018).
[11] Jing, Y., Sun, H., Zhang, L. and et al. “Variable speed control of wind turbines based on the quasi-continuous high-order sliding mode method”, *Energies*, **10**(10), p.1626 (2017).
[12] Beltran, B., Benbouzid, M.E.H. and Ahmed-Ali, T. “Second-order sliding mode control of a doubly fed induction generator driven wind turbine”, *IEEE Transactions on Energy Conversion*, **27**(2), pp.261-269 (2012).
[13] Sun, B., Sun, X.X. and Chen, L. “Discrete sliding mode control algorithm based on power function”, *Journal of Control and Decision*, **26**(2), pp.285-288 (2011).
[14] Gasmi, H., Mendaci, S., Laifa, S., and et al. “Fractional-order proportional-integral super twisting sliding mode controller for wind energy conversion system equipped with doubly fed induction generator”, *Journal of Power Electronics*, **22**(8), pp.1357-1373 (2022).
[15] Jabbour, N., Tsioumas, E., Mademlis, C., and et al. “highly effective fault-ride-through strategy for a wind energy conversion system with a doubly fed induction generator”, *IEEE Transactions on Power Electronics*, **35**(8), pp.8154-8164 (2020).
[16] Wang X, Li X, Zhang D, Wu T. “An improved global fast terminal high-order sliding mode control strategy based on novel reaching law for improving PMLSM dynamic performance”, *Energy Reports*, **9**, pp.829-838 (2023).
[17] Pyrkin, A., Bobtsov, A., Ortega. R., and et al. “Robust nonlinear observer design for permanent magnet synchronous motors”, *IET Control Theory & Applications*, **15**(4), pp.604-616 (2021).
[18] Susperregui, A., Martínez, M.I., Tapia-Otaegui, G., and et al. “Sliding-mode control algorithm for DFIG synchronization to unbalanced and harmonically distorted grids”, *IEEE Transactions on Sustainable Energy*, **13**(3), pp.1566-1579 (2022).
[19] Sun, X., Zhang, L., Gu, J. “Neural-network based adaptive sliding mode control for Takagi-Sugeno fuzzy systems”, *Information Sciences*, 628, 240-253 (2023).
[20] Zhang, Z., Guo, Y., Gong, D., and et al. “Global integral sliding-mode control with improved nonlinear extended state observer for rotary tracking of a hydraulic roofbolter”, *IEEE/ASME Transactions on Mechatronics*, **28**(1), pp.483-494 (2022)
[21] Usama, M., Kim, J. “Robust adaptive observer-based finite control set model predictive current control for sensorless speed control of surface permanent magnet synchronous motor”, *Transactions of the Institute of Measurement and Control*, **43**(6), pp.1416-1429 (2021).
[22] Nguyen, T.A., Nguyen, H.T., Phan, G.A., and et al. “An efficient model predictive control based on Lyapunov function for doubly fed induction generator fed by a T-type inverter”, *Electrical Engineering*, **103**, pp.663-676(2021).
[23] Döşoğlu MK. “Decoupled power-based sliding mode control modeling enhancement for dynamic stability in doubly-fed induction generator-based wind turbines”, *Computers and Electrical Engineering*, **104**, p.108448 (2022).

Mohammad Ali karami, received the B.S. and the M.S. degrees in electrical engineering from the Borujerd Branch, Azad University**,** Borujerd, Iran, in 2006 and 2014, respectively. He is a PhD student of electrical engineering at electrical engineering, Khomein, Iran. His research interests include artificial intelligence, optimization, and control systems.

S M Shariatmadar was born in Qom, Iran, in August 1973. He received the BSc degree from Tehran University, Tehran, Iran, in 1996, the MSc degree from the South Tehran Branch, Azad University, in 2003 and the PhD degree in electrical engineering at the Science and Research Branch, Islamic Azad University Tehran, Iran in 2011. His current research interests include modeling, analysis, and control of electrical machines, power electronic drives, and nonlinear phenomena in power electronics systems.

M.E. Nazari, received the M.S. and Ph.D. in electrical engineering from Amirkabir University of Technology (Tehran Polytechnic) in 2009 and 2016. Currently, he is an assistant professor of the electrical engineering at Isfahan University of Technology, Golpayegan College, Isfahan, Iran. His research interests include operation and economics of power systems

Javad Rahmani Fard received the B.S. degree from Shahed University, Tehran, Iran, in 2009, and the M.S. and Ph.D. degrees in electrical engineering from the K.N. Toosi University of Technology, Tehran, in 2012 and 2018, respectively. Currently, he is an assistant professor of the electrical engineering at Pooyesh Institute of Higher Education, Qom, Iran. His research interests include the analysis and design of electrical machines, and sensor-less variable-speed drives, multiphase variable-speed drives.

FIGURE CAPTIONS

Fig. 1. Spatial position between abc coordinate system and dq coordinate system.
Fig. 2. Block diagram of DFIG system based on power-function high-order sliding mode control
Fig. 3. Power functions, sign function and saturation functions curves.
Fig. 4. (a) Electromagnetic torque and (b) driving torque of DFIG system
Fig. 5. Tracking performance of active power based on (a) PI control and (b) high-order sliding mode control based on power function.
Fig. 6. The curve of active power variation when the rotor resistance changes in a DFIG system. (a) PI control and (b) high-order sliding mode control based on power function.
Fig. 7. Curves of active power and reactive power. (a) PI control and (b) high-order sliding mode control based on power function.
Fig.8. The physical experiment platform
Fig.9. Stator voltage and current under different wind speeds (a) n=1300r/min (b) n=1500r/min (c) n=1700r/min
Fig.10. Stator side power in steady state operation of grid
Fig.11. Change of rotor current waveform in the process of rotational speed change (a) n=700r/min-1700r/min (b) n=1700r/min-700r/min.
Fig.12. Voltage and current waveform of grid side under the change of speed (a) n=700r/min (b) n=1700r/min.
Fig.13. Active and reactive power waveforms on the stator side
Fig.14. Stator voltage and current waveform (a) Q=0var (b) Q=-500var (c) Q=500var.
Fig.15. Active and reactive power waveforms on the stator side

TABLE CAPTIONS

Table. 1 Parameters of DFIG
Table. 2 electrical parameters of doubly-fed wind power simulation system
Table. 3 Experimental parameters of steady state operation
Table 4. Experimental parameters of rotational speed changes
Table 5. Experimental parameters of active and reactive power decoupling control.

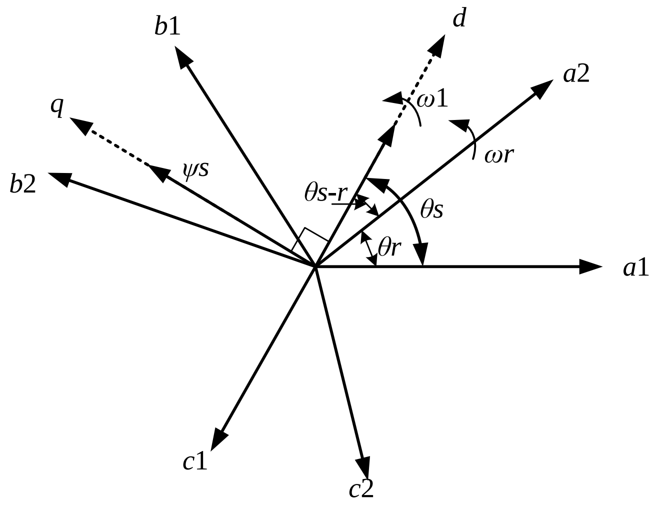

Fig. 1

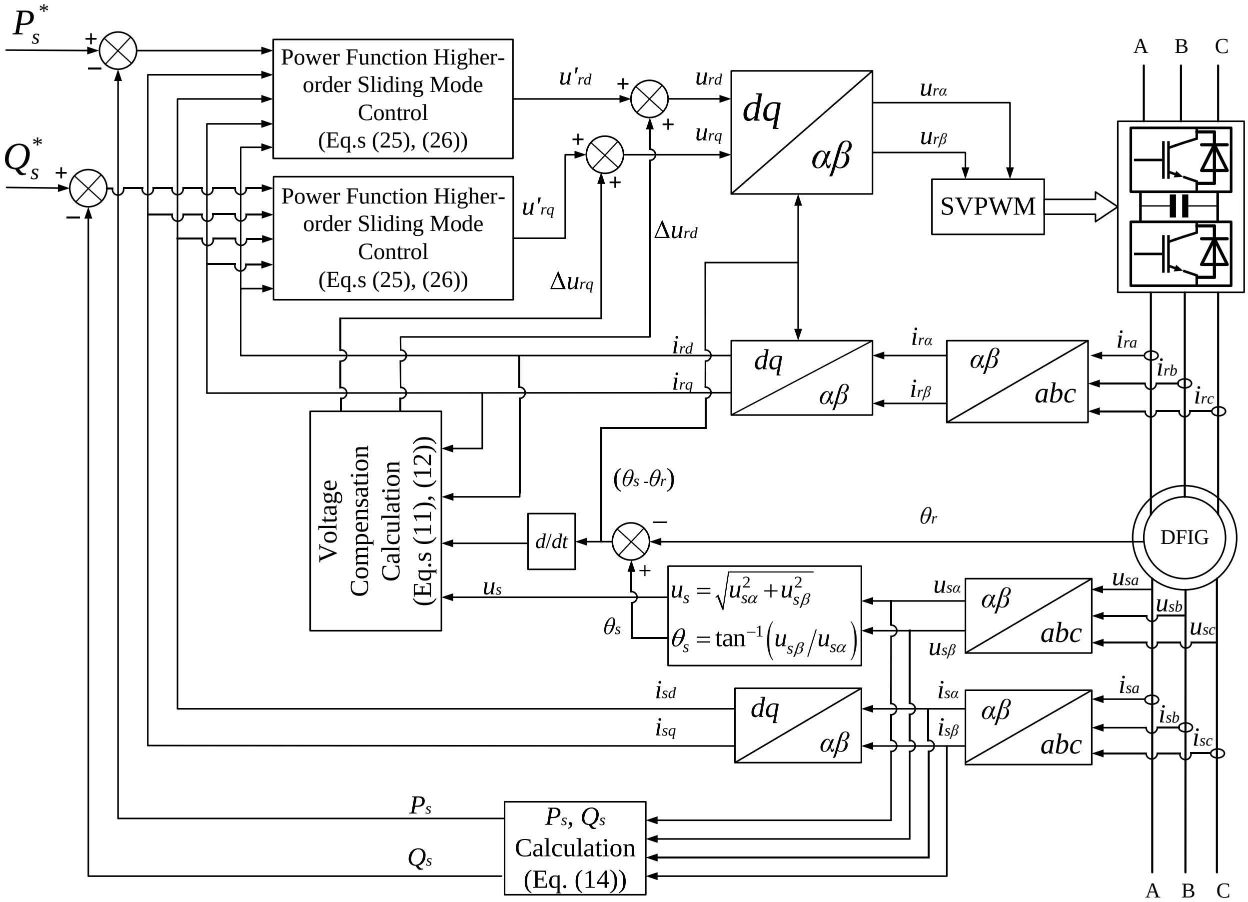

Power Function Higher-order Sliding Mode Control (Eq.s (25), (26))
Power Function Higher-order Sliding Mode Control (Eq.s (25), (26))
dq
αβ
SVPWM
A B C
Voltage Compensation Calculation (Eq.s (11), (12))
d/dt
(θs -θr)
θr
DFIG
Ps, Qs Calculation (Eq. (14))
Ps
Qs

Fig. 2

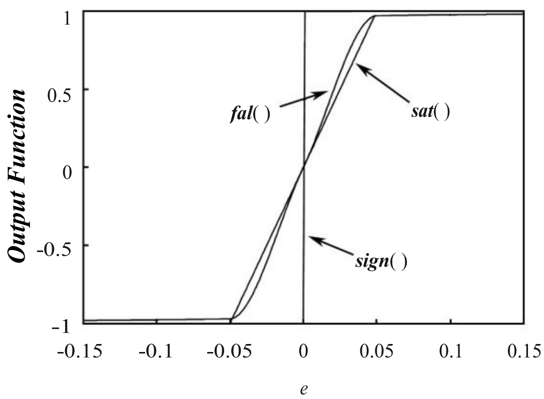

Output Function
fal( )
sat( )
sign( )
e

Fig. 3

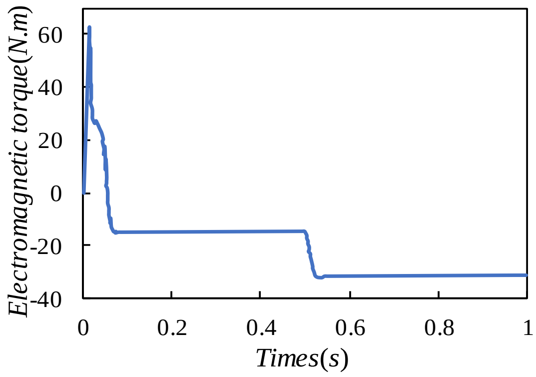
Electromagnetic torque(N.m)
60
40
20
0
-20
-40
0
0.2
0.4
0.6
0.8
1
Times(s)

(a)

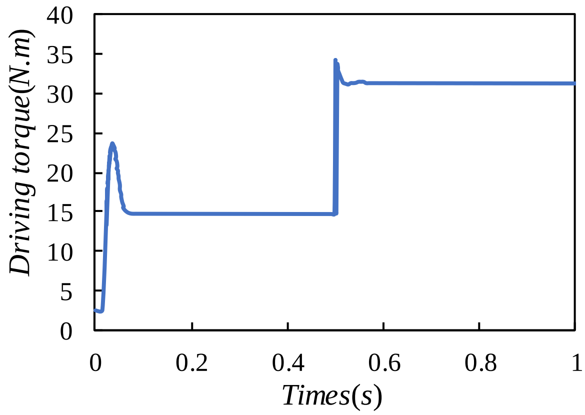
Driving torque(N.m)
40
35
30
25
20
15
10
5
0
0
0.2
0.4
0.6
0.8
1
Times(s)

(b)

Fig. 4

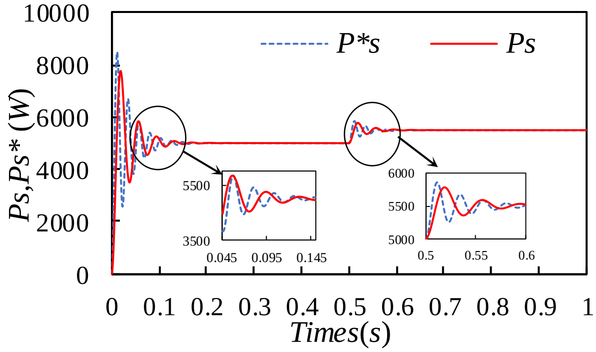

(a)

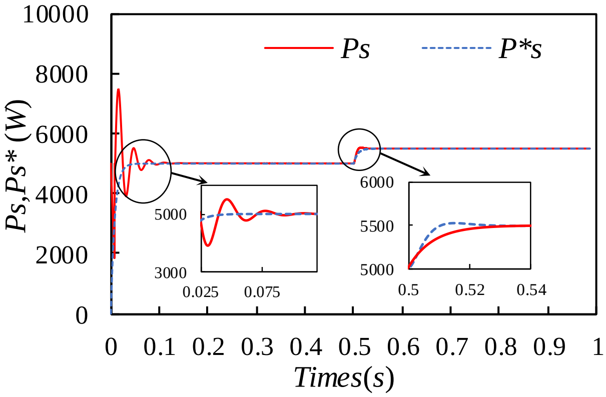

(b)

Fig. 5

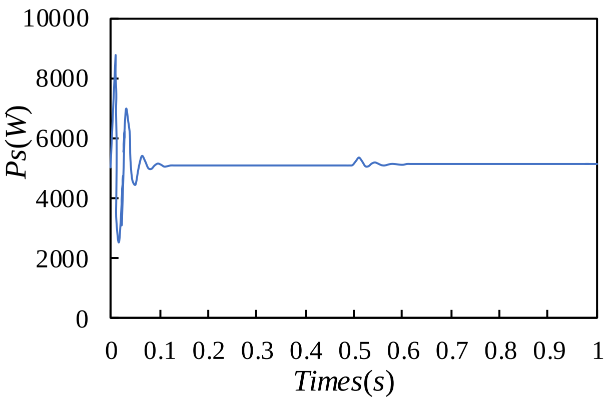

(a)

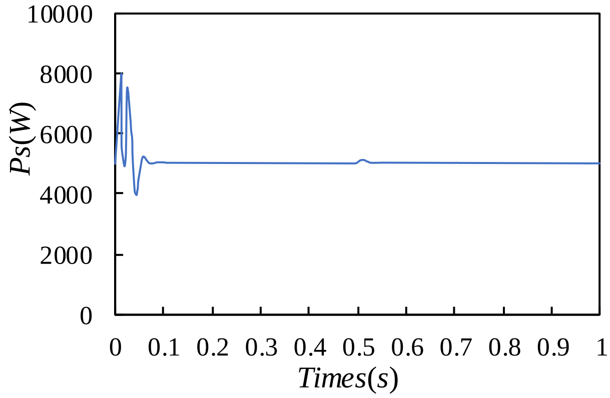

(b)

Fig. 6.

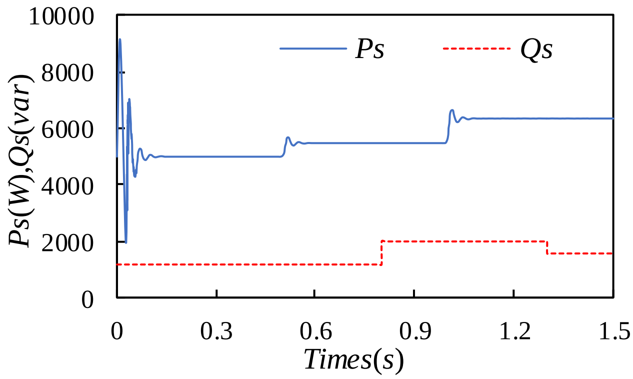

(a)

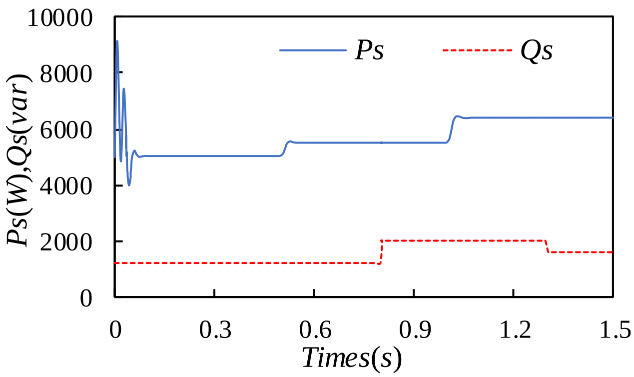

(b)

Fig. 7.

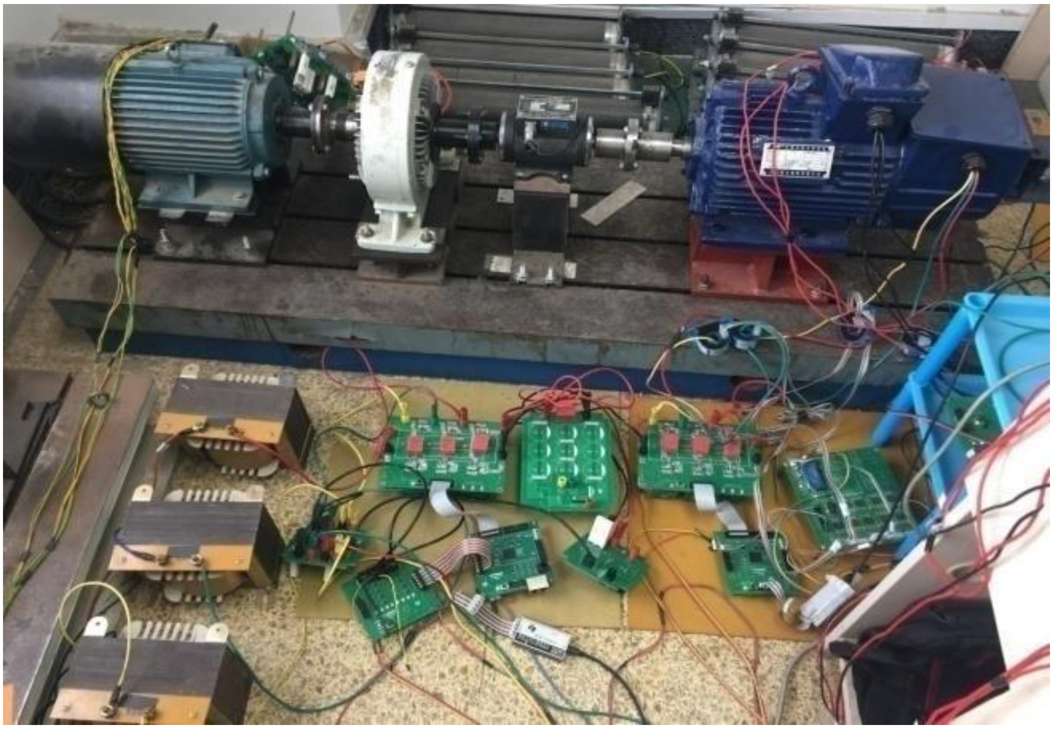

Fig.8

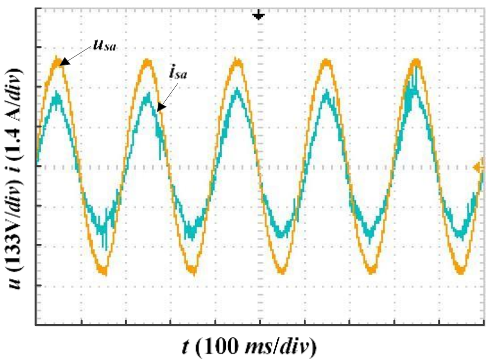

u_{sa}
i_{sa}
u (133V/div) i (1.4 A/div)
t (100 ms/div)

(a)

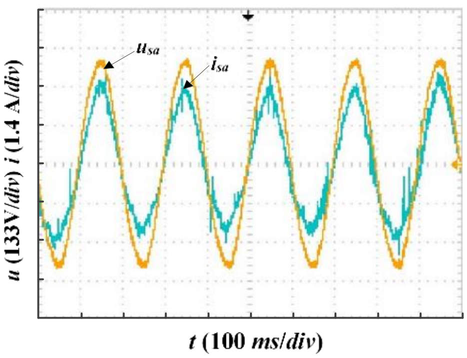

u_{sa}
i_{sa}
u (133V/div) i (1.4 A/div)
t (100 ms/div)

(b)

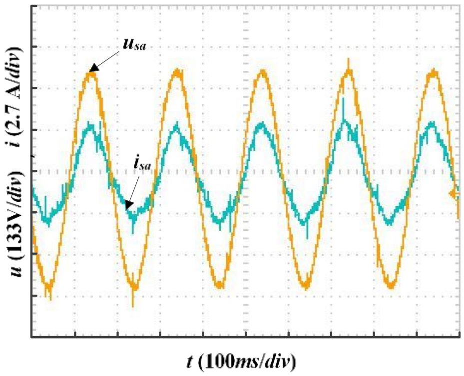

(c)

Fig.9

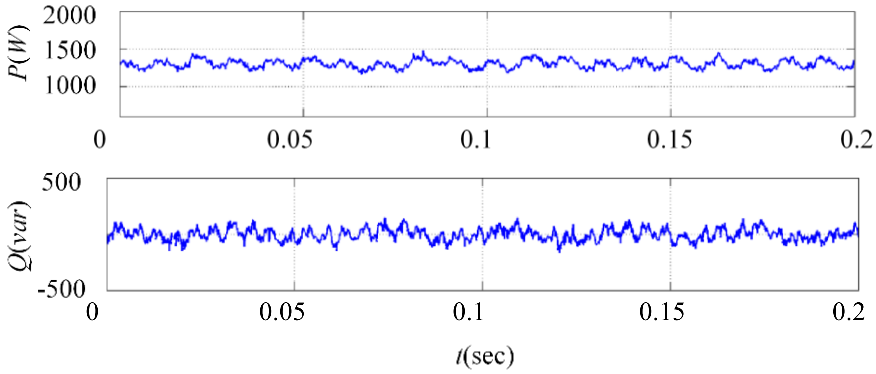

Fig.10

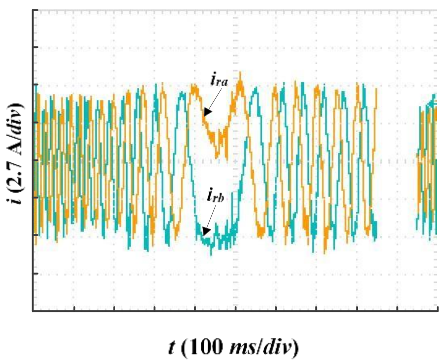

(a)

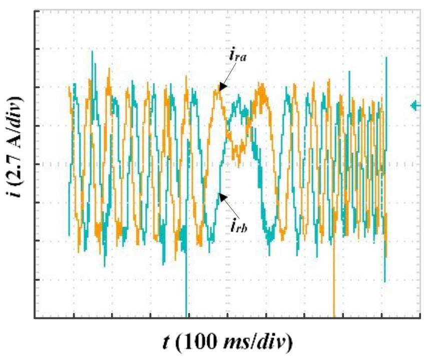

(b)

Fig.11

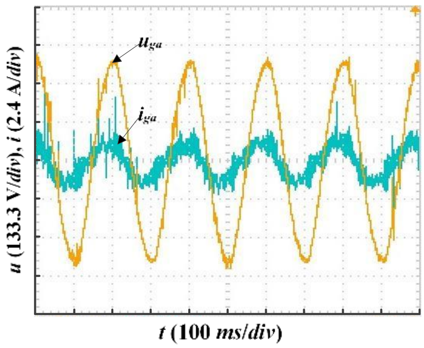

(a)

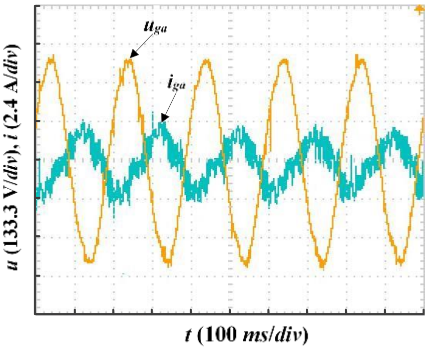

(b)

Fig.12

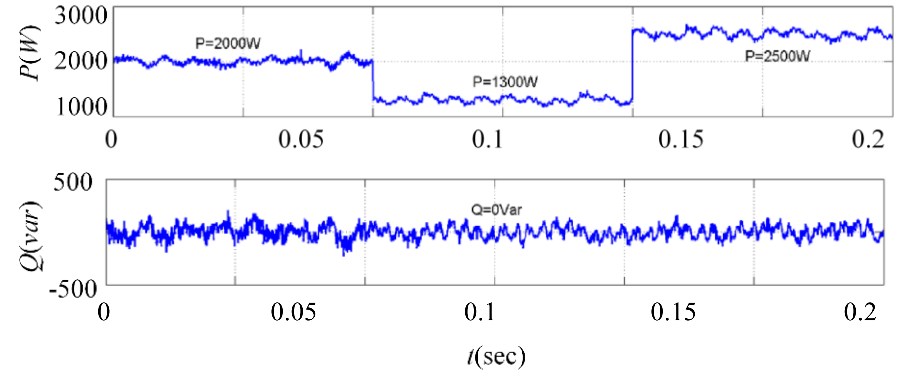

Fig.13

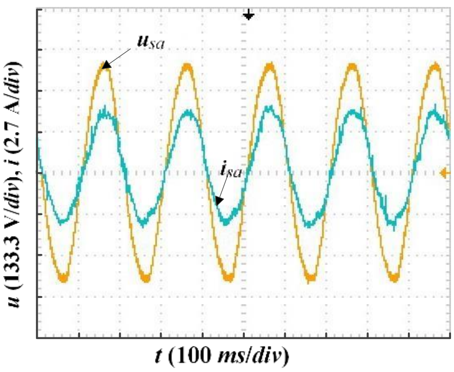

(a)

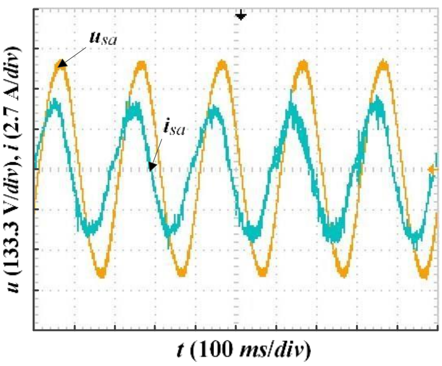

(b)

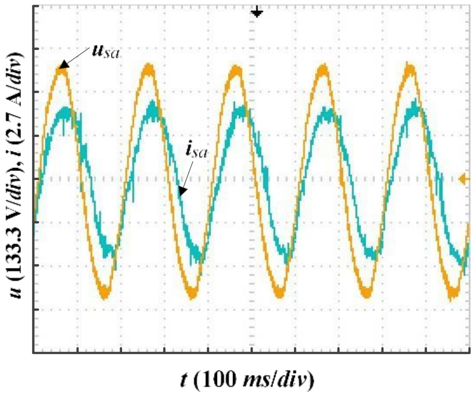

(c)

Fig.14.

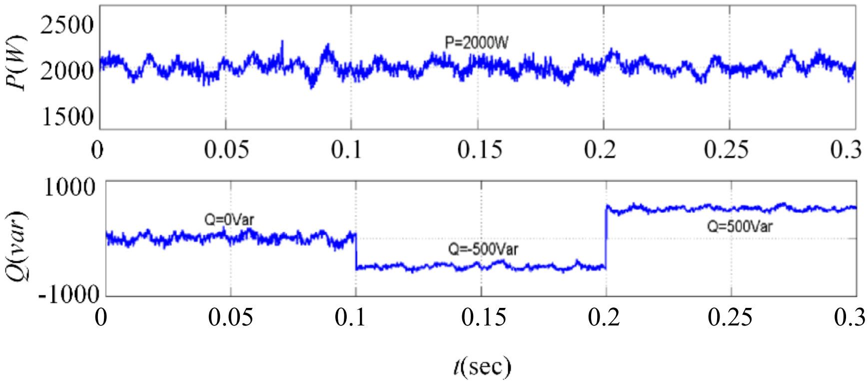

Fig.15

Table. 1

Item	*Symbol*	Value
Optimal wind energy utilization coefficient	C_{pmax}	0. 48
Optimum tip speed ratio	λ_m	8. 1
Gearbox speed ratio	k	5. 4
Blade radius	R	2. 1m
Number of pole pairs	n_p	2
Air density	ρ	1. 25kg/m^3
Motor stator resistance	R_s	1. 92Ω
Motor rotor resistance	R_r	2. 58Ω
Stator and rotor self-inductance	L_s, L_r	0. 25 H
Mutual inductance	L_m	0. 15 H
Mains voltage	U	380 V
Moment of inertia	J	0. 2kg/m^2

Table. 2

Item	Symbol	Value
U	0V~220V	Grid side AC input voltage effective value (adjustable)
f	50Hz	grid voltage frequency
L	4mH/50A	grid side filter inductor
C	470uF/1350V	DC bus capacitor
f_e	5kHz	PWM switching frequency
T	380V: 380V	Transformer JH-TDB-SPD

Table. 3

Name	parameter
Sub-synchronous wind speed	1300r/min
Synchronous wind speed	1500r/min
Super synchronous wind speed	1700r/min
Active power given	1300W
Reactive power reference	0VAR

Table 4.

Name	parameter
Sub-synchronous to super-synchronous step wind speed change	700r/min-1700r/min
Super-synchronous to sub-synchronous step wind speed change	1700r/min-700r/min
Active power set point	1300W
Reactive power set point	0VAR

Table 5.

Name	Parameter
Wind speed set point	1300r/min
Active power set point	1300-2500W
Reactive power set point	±500VAR